Ceramic composites based on $Ca_3Co_{4-x}O_{9+\delta}$ and $La_2NiO_{4+\delta}$ with enhanced thermoelectric properties

R. Hinterding [a],[*], Z. Zhao [a], M. Wolf [a], M. Jakob [b], O. Oeckler [b], A. Feldhoff [a],[**]

[a] Leibniz University Hannover, Institute of Physical Chemistry and Electrochemistry, Callinstr. 3A, D-30167, Hannover, Germany
[b] Leipzig University, Institute of Mineralogy, Crystallography and Materials Science, Scharnhorststr. 20, D-04275, Leipzig, Germany

ARTICLE INFO

ABSTRACT

Ceramic composites were produced by combining the oxide materials $Ca_3Co_{4-x}O_{9+\delta}$ and $La_2NiO_{4+\delta}$. Both compounds were characterized by a plate-like crystal shape, but crystal sizes differed by around two orders of magnitude. The composite materials could be successfully prepared by using uniaxial pressing of powder mixtures and pressureless sintering to a porous ceramic. Possible reactions between both materials during sintering were analyzed. The ceramic composites with low amounts of $La_2NiO_{4+\delta}$ showed enhanced thermoelectric properties, caused by an increasing power factor and simultaneously decreasing thermal conductivity. For the evaluation of the thermoelectric properties, two different types of Ioffe plots were utilized. The maximum figure-of-merit zT at 1073 K was 0.27 for the pure $Ca_3Co_{4-x}O_{9+\delta}$ as well as for the sample containing 5 wt% $La_2NiO_{4+\delta}$. However, the average $\overline{ZT}$ in the temperature range of 373 K to 1073 K could be increased by 20% for the composite material.

1. Introduction

1.1. Thermoelectric energy conversion

In the light of limited resources, energy harvesting is a topic with increasing importance. A promising option is the conversion of wasted thermal energy into electrical energy via thermoelectric generators. However, the efficiency and performance of the latest thermoelectric materials still require further research to allow widespread application. There are various material classes such as tellurides [1], half-Heusler compounds [2], Zintl phases [3], polymers [4], oxides [5], oxy-selenides [6] and many more, which all have their advantages and dis-advantages with respect to efficiency, energy conversion, chemical stability, application temperature or toxicity. Especially the working temperature and atmosphere are usually important criterions when choosing the proper thermoelectric materials for an application. For high-temperature applications with working conditions in air, the chemical stability of the used materials can be challenging. However, oxides typically show high temperature stability in air and especially the *p*-type cobalt oxide $Ca_3Co_{4-x}O_{9+\delta}$ (CCO) also shows remarkable thermoelectric properties based on its layered structure [5,7]. CCO is stable up to approximately 1200 K under air [8,9] and has a monoclinic crystal

structure built up from two incommensurate subsystems [10]. One sub-system contains CoO_2 as a misfit-layered CdI_2 structure type and the other subsystem consists of three Ca_2CoO_3 units as a layered cutout of the rock-salt type. Both subsystems alternate along the shared *c*-axis with same *a* and distinct *b* lattice parameters [11].

To discuss the performance of thermoelectric materials, some fundamental parameters appearing in the thermoelectric material tensor of Eq. (1) are indispensable [12–14].

$$\begin{pmatrix} I_q \\ I_S \end{pmatrix} = \frac{A}{L} \begin{pmatrix} \sigma & \sigma \cdot \alpha \\ \sigma \cdot \alpha & \sigma \cdot \alpha^2 + \Lambda \end{pmatrix} \cdot \begin{pmatrix} \Delta\phi \\ \Delta T \end{pmatrix} \quad (1)$$

The thermoelectric energy conversion of a thermoelectric material with a cross-sectional area *A* and a length *L* relies on the coupling of currents of electrical charge I_q and entropy I_S. Under the assumption of constant gradients, the electrical potential difference $\Delta\phi$ and the temperature difference ΔT may cause a thermally-induced electrical current, which is dependent on the three material parameters: the isothermal electrical conductivity σ, the Seebeck coefficient α and the electrically open-circuited entropy conductivity Λ. The entropy conductivity is directly related to the open-circuited heat conductivity λ via Eq. (2), and both can be addressed by the term thermal conductivity [15]. The thermoelectric parameters all reappear in Eq. (2), where the performance of a

---

thermoelectric material is given by the figure-of-merit zT.

$$zT = \frac{\sigma \cdot \alpha^2}{\lambda} \cdot T = \frac{\sigma \cdot \alpha^2}{\Lambda} = \frac{PF}{\Lambda} \tag{2}$$

One advantage of using the more fundamental entropy conductivity is making the figure-of-merit explicitly dependent on all three material parameters but only implicitly on temperature [14]. While the zT describes the maximum energy conversion efficiency, the power factor $PF = \sigma \cdot \alpha^2$ is proportional to the maximum electrical power output of a thermoelectric material. Both quantities are important to describe the thermoelectric performance of a material [15].

1.2. Thermoelectric composites

Composite materials can combine specific single phase properties into a superior heteromaterial. The influence of introducing one or multiple phases to a main matrix material is highly dependent on the chosen materials. In general, the introduction of heterointerfaces can affect the mean-free path of phonons and hence the thermal conductivity [16–18]. Material combinations comprising organic polymers and inorganic materials showed success in increasing the Seebeck coefficient of the system significantly [19–21]. Other composites introduce carbon nanotubes to benefit from a higher electrical conductivity [22,23]. Regarding CCO, the addition of Ag inclusions has shown beneficial effects on the thermoelectric performance [24–26]. Furthermore, adding polymers to gain a triple-phase CCO/Ag/polymer composite could reduce the thermal conductivity considerably, but the material combination made proper sintering difficult [27]. Another composite consisting of the three phases CCO, Na_xCoO_2 and $Bi_2Ca_2Co_2O_9$ was gained by using high dopant levels of Na and Bi during the synthesis [28]. This composite benefitted from similar layered crystal structures of the components and resulted in an increased power factor. It also shows the benefits of combining doping and composite materials, which was also investigated for Ag doping and Ag inclusions by Wang et al. [29]. Generally, doping is a powerful instrument for improving thermoelectric properties of CCO. The currently best figure-of-merit zT for polycrystalline CCO was reached by Saini et al. [30] with 0.74 at 800 K by Tb doping. Some other promising doping elements leading to improved thermoelectric properties are Bi [31], Ag [29], Fe [32], Eu [33] or Lu [34]. A zT value of 0.87 at 973 K was reached for the single-crystalline material [35], but polycrystalline materials are preferred in terms of synthesis effort.

Regarding the thermoelectric properties of a two-phase composite, Bergman et al. stated some theoretical limits [36]. While the figure-of-merit shall not be able to exceed the zT value of the pure single components, this is not applicable for the power factor [37]. However, these studies were made before the more recent development regarding influences on the nanoscale. Furthermore, partial reactions between the components may lead to a multiphase system, which impair the validity of these statements in that case.

Within this study, the combination of CCO and $La_2NiO_{4+\delta}$ (LNO) to CCO/LNO ceramic composites was investigated. While most research on CCO focuses on thermoelectrics, the mixed ionic-electronic conductivity and dielectric properties of LNO make it interesting for several potential applications in microelectronics, gas separation membranes or catalysis [38–40]. It is a p-type material with a moderate Seebeck coefficient of approximately 50 μV K^{-1} at 1273 K, which can increase significantly in dependence of oxygen partial pressure and hole doping [41,42]. The heat conductivity decreases with temperature and is about 5.5 W m^{-1} K^{-1} at 1000 K [43] while the electrical conductivity can reach values up to 200 S cm^{-1} [44]. The structure of LNO comprises LaO rock-salt layers and $LaNiO_3$ perovskite layers, which alternate along the c-axis [45,46]. Therefore, both mixing components are characterized by layered structures and anisotropic transport properties, making it important to combine the properties in the same direction. The good electrical conductivity and the shared p-type conductivity make the LNO suitable as a mixing partner

within a CCO matrix. As high sintering temperatures were used, reactions between the CCO and LNO phases are possible and were investigated. The aim of preparing the CCO/LNO ceramic composites was the increasement of the thermoelectric properties in comparison to pure CCO. To evaluate these properties, two different Ioffe plots regarding the power factor and the entropy conductivity were used [15,47].

2. Experimental

2.1. Materials

Two different oxide powders were used to produce ceramic oxide composites. The calcium cobalt oxide $Ca_3Co_{4-x}O_{9+\delta}$ (CCO) powder was purchased from CerPoTech (Tiller, Norway). The lanthanum nickelate $La_2NiO_{4+\delta}$ (LNO) was synthesized by introducing oxide mixtures of La_2O_3 and NiO into an alumina crucible with NaOH pellets, followed by heating at 673 K for 8 h with a heating rate of 10 K min^{-1}. The mixture was cooled to room temperature and washed with distilled water and acetone. Since the LNO is based on a previous work, more detailed information about the synthesis process can be found there [38]. Composites of CCO and LNO were synthesized by mixing the powders in the respective weight ratios of 99:1, 95:5, 90:10, 80:20 and 60:40 to a total weight of 1 g. The mixture was ground in an agate mortar for approximately 15 min and uniaxially pressed in a 16 mm die with 250 MPa at room temperature. Afterwards, pressureless sintering to ceramic samples was processed at 1173 K for 10 h with a heating and cooling rate of 2 K min^{-1} under air. For thermoelectric measurements, the sintered disks were cut into bars with a length of 10 mm by using a precision vertical diamond wire saw from O'Well model 3242.

2.2. Analysis of microstructure

To investigate the phase purity of used powders and gained ceramics, X-ray diffraction (XRD, Bruker AXS GmbH, Bruker D8 Advance) measurements were operated in a step-scan mode between 10° and 80° 2θ with a step size of 0.01° and 1 s per step without sample rotation. Cu-K$_\alpha$ radiation was used at 40 kV and 40 mA. Powder diffraction data for identification and comparison within this work are used for the compounds $Ca_3Co_{4-x}O_{9+\delta}$ (Miyazaki et al. [11], monoclinic, $a = 4.834$ Å, $b_1 = 2.824$Å, $b_2 = 4.558$Å, $c = 10.844$ Å), $Ca_3Co_2O_6$ (PDF: [01-089-0630], rhombohedral, $a = 9.079$ Å, $c = 10.381$ Å), Co_3O_4 (PDF: [01-073-1701], cubic, $a = 8.084$ Å), $La_2NiO_{4+\delta}$ (PDF: [01-078-2186], tetragonal, $a = 5.502$ Å, $c = 12.504$ Å), La(Co,Ni)O$_3$ (PDF: [00-054-0834], rhombohedral, $a = 5.465$ Å, $c = 13.125$ Å). The incommensurate structure of CCO required the approach of a four-dimensional superspace group for indexing the X-ray and electron diffraction patterns. Therefore, the superspace group Cm (0 1 - p 0) (equivalent to Bm (0 0 γ) No. 8.3) was applied in accordance with literature [11,48,49].

A field-emission scanning eletron microscope (SEM, JEOL JSM-6700F) was used for micrographs at 2 kV and elemental mappings at 15 kV with the equipped energy dispersive X-ray spectrometer (EDXS, Oxford Instruments, INCA-200). In-depth analysis of the composition was accomplished by a field-emission transmission electron microscope (TEM, JEOL JEM-2100F-UHR), which was also equipped with an EDXS (Oxford Instruments, INCA-300). Scanning TEM (STEM), high-resolution TEM (HRTEM) and selected area electron diffraction (SAED) were made at 200 kV. Density and porosity of the sintered disks were determined by the Archimedes method (ISO 5018:1983). Isopropanol was used as a fluid and density values were averaged for three different disks resulting in deviations of up to 2%.

2.3. Analysis of thermoelectric properties

Measurements of the electrical conductivity σ, the Seebeck coefficient α and the heat conductivity λ were realized with respect to temperature

dependency and orientation of the samples. The sintered ceramics were cut into bars (10 mm, 2 mm, 1.6 mm) to measure the electrical conductivity and the Seebeck coefficient perpendicular to the pressing direction. The measurement of the electrical conductivity was accomplished by a 4-point probe method at equilibrium conditions within a horizontal three-heating-zone tube furnace from Carbolite Gero EVZ 12/450B. To measure the Seebeck coefficient, a ProboStat A setup from NorECs with a vertical furnace from Elite Thermal Systems Ltd. at equilibrium conditions was used. Measurements were done with KEITHLEY multimeters and gained data processed by using Lab VIEW software. Equilibrium conditions were reached by heating the samples to 1073 K and measuring downwards with set up heating plateaus every 100 K. A laser flash setup LFA 1000 from Linseis with an InSb detector was used to measure the thermal diffusivity D under an oxygen-helium mixed atmosphere (80% He, 20% O_2). Test measurements without oxygen partial pressure resulted in a decomposition of CCO between 773 K and 873 K [50], wherefore the mixture was necessary to gain reliable data. Values for the heat capacity of CCO were taken from a former publication [28] and the CCO/LNO ceramic composites were measured in relation to the CCO. Two different sample orientations as perpendicular and parallel to the pressing direction were investigated. The measurements perpendicular to the pressing direction were conducted up to 573 K. The limitation in temperature was caused by the used lamellar graphite holder from Linseis, which is not stable in an oxidic atmosphere at high temperatures. For using the lamellar holder, cut bars were rotated by 90° and aligned. The utilization of the holder was essential and enabled measurements of the thermal diffusivity in the same direction as the electrical conductivity and the Seebeck coefficient and therefore a determination of figure-of-merit zT. Values of thermal diffusivity above 573 K with orientation perpendicular to the pressing direction were estimated by calculating polynomial fits for the measurements parallel to the pressing direction. As these parallel measurements were conducted in the full temperature range of 373 K–1073 K, their fits were transferred to the measurements in the other direction assuming similar trends.

3. Results and discussion

3.1. Ceramic composite: microstructure

For obtaining the ceramic composites, two different oxide powders consisting of $Ca_3Co_{4-x}O_{9+\delta}$ (CCO) and $La_2NiO_{4+\delta}$ (LNO) were used. Phase purity and crystal shape of these compounds have been confirmed by powder XRD patterns and SEM micrographs (compare Fig. S1). The CCO showed 30 nm thin sheets with extensions about 200–500 nm and the LNO large plate-like or cuboidal particles with several microns in size. The XRD patterns showed the reflections of the desired phases with negligible impurities of Co_3O_4 in case of the CCO.

Regarding the CCO/LNO ceramic composites after sintering, the XRD patterns are displayed in Fig. 1a. For a more precise comparison, enlarged graphs are given in Fig. S2. No additional reflections could be detected for the samples with up to 10 wt% LNO, but for 20 wt% and 40 wt% LNO reflections of $Ca_3Co_2O_6$ and the perovskite phase $La(Co,Ni)O_3$ became apparent. Together with the lack of $La_2NiO_{4+\delta}$ reflections in all samples, this indicates a reaction between CCO and LNO has occurred. The density measurements in Fig. 1b show a bulk density of 2.94 g cm^{-3} for pure CCO, which results in a relative density of 63% in comparison to the theoretical density of 4.68 g cm^{-3} [51]. The bulk density of the ceramic composites increased linearly with the added amount of LNO, which can be explained by the higher density of 7.32 g cm^{-3} for LNO or 7.23 g cm^{-3} for LaNiO$_3$. By extrapolating the linear fit to 100% LNO, it does not reach a value of dense LNO, because higher sintering temperatures of at least 1473 K would be required [52], but CCO decomposes at temperatures above roughly 1200 K in air [8,9].

To examine the absence of LNO reflections in the XRD patterns after sintering, SEM-EDXS analysis of the sample with 5 wt% LNO was done. Fig. 2 shows the microstructural characterization of a single LNO particle
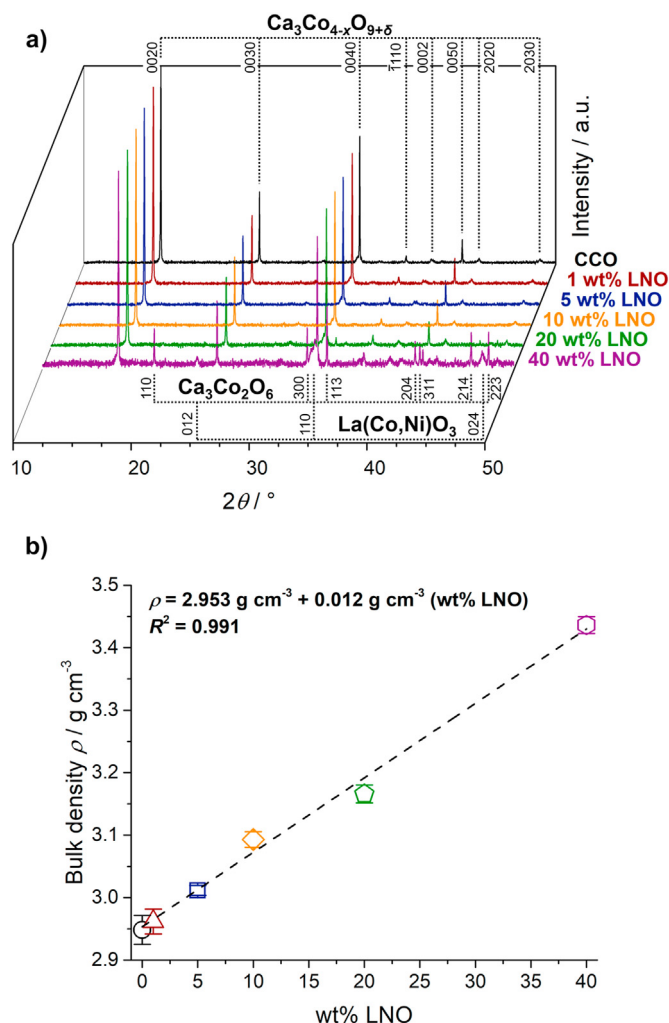

Fig. 1. Composition and density of the CCO/LNO ceramic composites after sintering. a) Background-corrected and normalized XRD patterns of the matrix material CCO and the composites with indexed reflections for the CCO and the phases of reaction sintering $Ca_3Co_2O_6$ and $La(Co,Ni)O_3$. Reflections of CCO were indexed with the four-dimensional superspace group approach [11]. b) Densities of the CCO and the composites determined by Archimedes method. The bulk density shows a linear dependency on the added amount of LNO.

inside the CCO matrix (compare Fig. S3 for an overview of the LNO distribution). Concerning the elemental distributions in Fig. 2d–h several things are worth highlighting. First of all, the lanthanum is solely located within the original LNO particle and did not diffuse into the CCO matrix. Cobalt on the other hand did penetrate the LNO particles and some cobalt-nickel inclusions are visible as well. Depending on the penetration depth from the polishment, these inclusions could also be located at the surface of the particle. This assumption is encouraged by the same cobalt-nickel rich phase surrounding the particle. The calcium is mainly located within the CCO matrix. With the knowledge from the XRD patterns, the newly formed $La(Co,Ni)O_3$ has to be located within the LNO particle and the $Ca_3Co_2O_6$ most likely in its vicinity. The formation of $La(Co,Ni)O_3$ is confirmed by comparing the La:Ni ratio before and after the sintering by a quantitative EDXS analysis. A detailed description of the investigated areas and resulting elemental compositions is given in Fig. S4. Before sintering the ratio was about 2:1 as confirmed by previous studies [38], but afterwards it changed significantly to 2:0.7. Interestingly, the La:Co ratio even reached a value of 2:1.5, wherefore the La:(Co,Ni) ratio is roughly 1 and therefore matching to the perovskite compound. The loss of Ni within the particle could also be the reason for the formation of the cobalt-nickel rich phase, which was not detected by XRD and needs
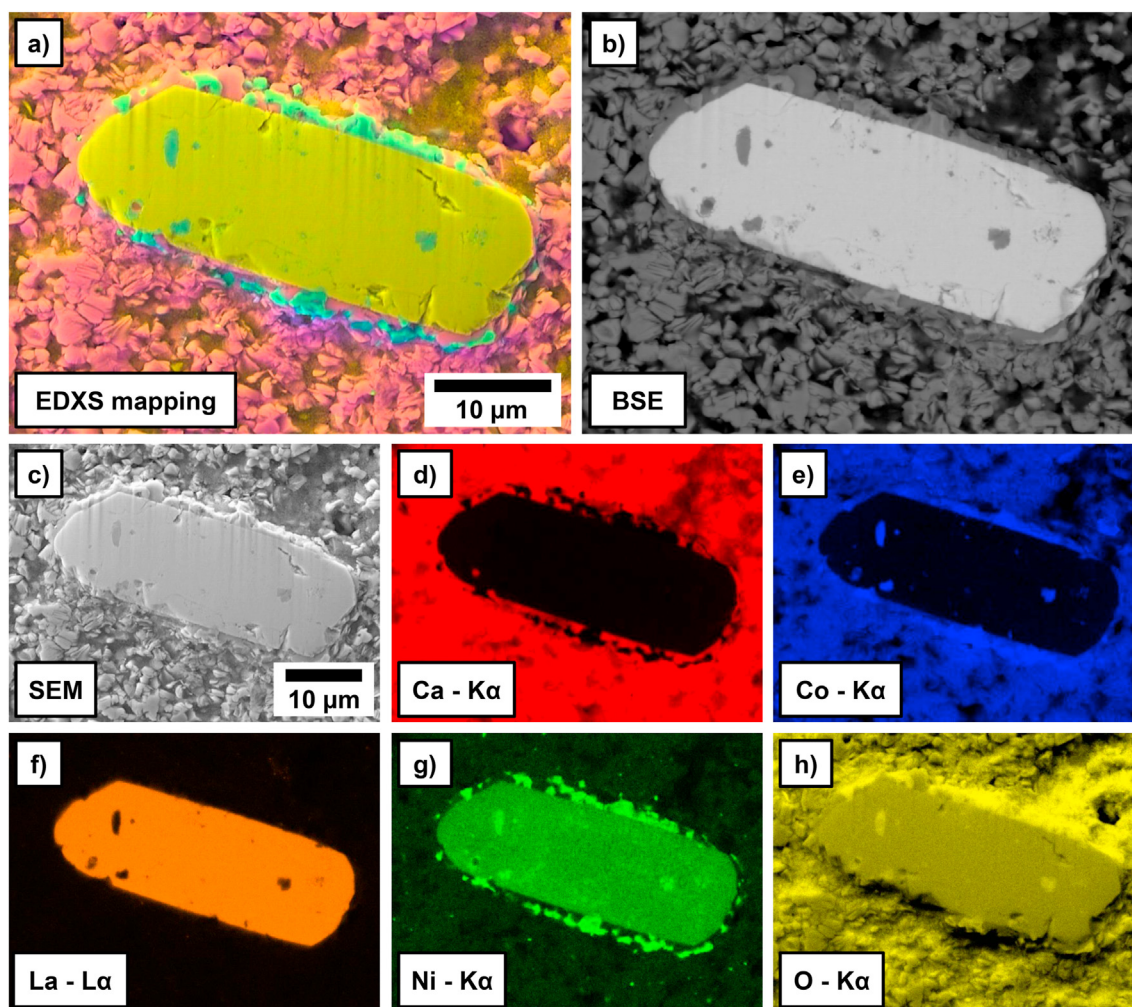
Fig. 2. Cross-sectional SEM-EDXS analysis of the 5 wt% LNO sample after sintering showing a single LNO plate-like crystal embedded in a CCO matrix. a) Overlay EDXS mapping and corresponding SEM micrograph summarizing the results from c-h. b) Backscattered-electron (BSE) micrograph showing the elemental contrasts. c) SEM micrograph as basis for EDXS analysis. d-h) Elemental distributions of the respective elements Ca, Co, La, Ni and O. Note, for the oxygen distribution shading effects are visible, caused by surface irregularities.

further analysis provided by TEM measurements in the following.

Firstly, the CCO matrix within the 5 wt% LNO sample was investigated by TEM and its results can be seen in Fig. 3. The STEM micrographs in Fig. 3a and b shows lamellar contrasts, which are attributed to stacking faults. The EDXS mapping in Fig. 3c shows a homogeneous distribution of calcium and cobalt and therefore no unwanted inclusions. The HRTEM micrograph in Fig. 3d shows stacked layers, fitting to the layered structure of CCO along the *c*-axis. The stacking faults become apparent in the SAEDs of Fig. 3e–g along the [1100] zone axis. The SAED pattern becomes distinct when a single lamella is investigated in Fig. 3e, but at the interface of the lamellae the reflections of the [$\bar{1}$100] zone axis also appear. This is typical for microtwins, where the stacking order is inversed [53]. A direct comparison between the experimental and the simulated SAED patterns for the microtwin is given in Fig. 3g and h. The resulting orientation relationship between the two grains called A and B is therefore $[1100]_A \parallel [\bar{1}100]_B \wedge (0010)_A \wedge (0010)_B$. This characteristic was found frequently within the sample and is to our best knowledge not yet reported for CCO. It is most likely attributed to the synthesis technique, wherefore it could not be further influenced. The investigation of the matrix shows the CCO being unimpaired from the LNO as long as its not in direct contact with it.

Secondly, the CCO-LNO interface has been analyzed via STEM, EDXS and SAED, shown in Fig. 4a–e. The EDXS analysis confirms the results

from the SEM in terms of cobalt diffusing into the LNO. Since CCO is the only possible cobalt source within the composite, the CCO has to decompose into $Ca_3Co_2O_6$ by releasing CoO and O_2 [54,55]. Surprisingly, not only the direct interface but the whole LNO particle shows significant amounts of cobalt. This explains the disappearing XRD reflections of LNO and the appearing reflections of $La(Co,Ni)O_3$ discussed formerly in Fig. 1a. As the oxidation state of Ni is increased in $La(Co,Ni)O_3$ compared to $La_2NiO_{4+\delta}$, the involvement of atmospheric oxygen is likely. Furthermore, the polycrystalline nature of the $La(Co,Ni)O_3$/LNO particles become evident by looking at the SAEDs of Fig. 4d and e. While some distinct patterns could be detected for $La(Co,Ni)O_3$ and LNO along the [001] zone axis, several other reflections are visible as well. This means the introduction of cobalt into the LNO led to a breakdown of the original crystal structure and the formation of a polycrystalline system with $La(Co,Ni)O_3$ as the main phase and LNO as a minor phase existing next to each other. Another phase needing clarification from Fig. 2 is the nickel-cobalt rich phase. In Fig. 4f–i, this phase could be identified as NiO with high amounts of Co, resulting in (Ni,Co)O with a Ni:Co ratio of 1:0.6 based on the EDXS analysis. The phase was located close to the LNO particles, but not at the direct interface of CCO-LNO, which means it could be caused by nanocrystalline NiO particles on the compound LNO, which were not detectable by XRD. A more reasonable explanation supported by the EDXS results of Fig. 2 is the formation of NiO as a result of the reduced La:Ni ratio within $La(Co,Ni)O_3$ in comparison to LNO. The
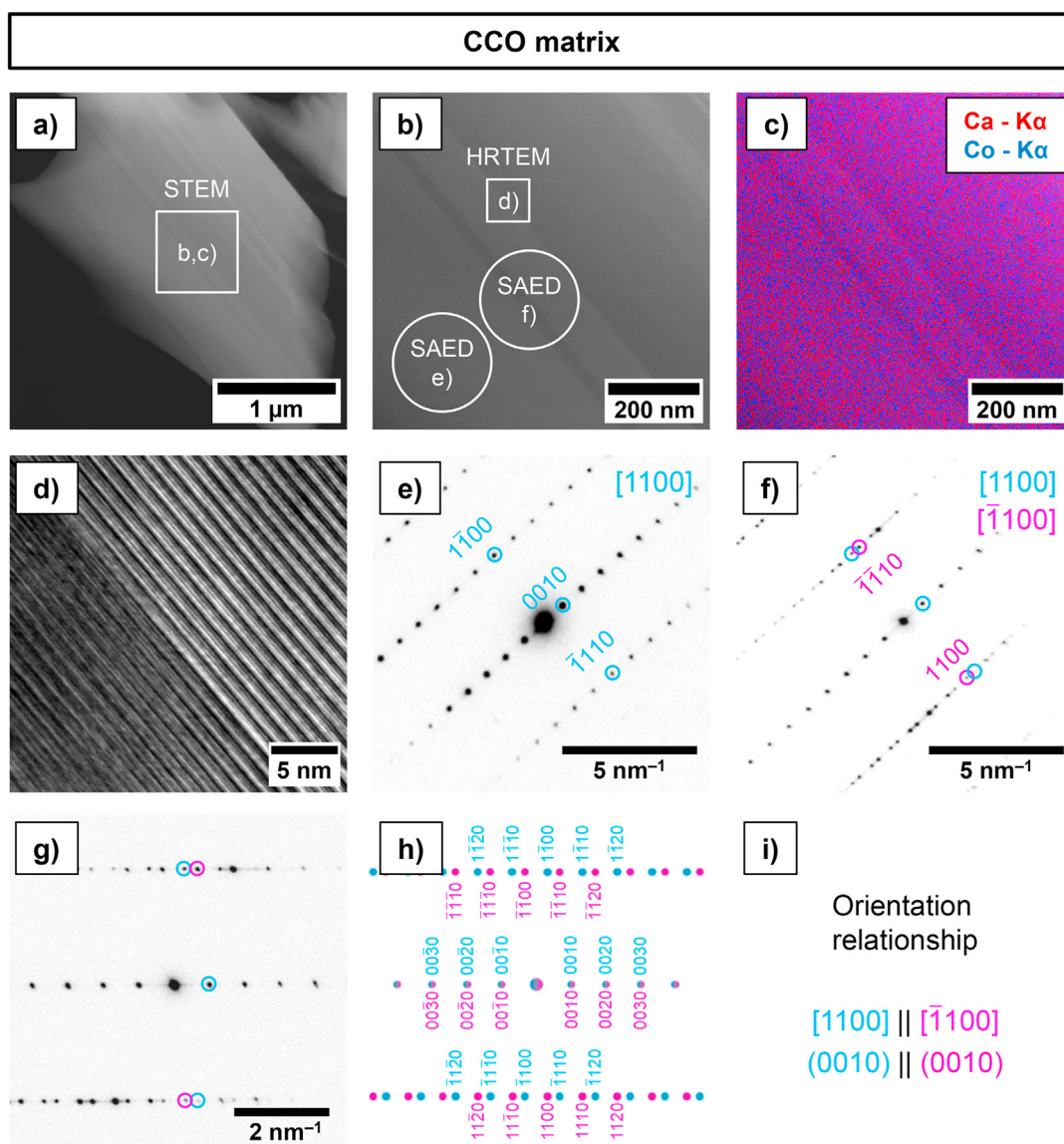
Fig. 3. Cross-sectional TEM characterization of the CCO matrix within the sample of 5 wt% LNO. a,b) STEM annular dark-field micrographs showing lamellar contrasts and the SAED scanning area size. c) EDXS mapping of the CCO to prove the homogeneous distribution of the elements Ca and Co. d) High-resolution TEM highlighting the stacking of the layered structure at the grain boundary. e) SAED pattern of the [1100] zone axis with given Laue indices. f) SAED pattern at the grain boundary, which shows reflections along the [1100] and [$\bar{1}$100] zone axes, indicating microtwins. g) Enlarged and rotated SAED pattern of f) for an easy comparison with the simulated pattern in h). h) Simulated SAED patterns of the [1100] and [$\bar{1}$100] zone axes. i) Resulting orientation relationship at the grain boundary. Reflections of CCO were indexed with the four-dimensional superspace group approach [11].

segregated Ni could therefore be responsible for the NiO formation in the vicinity of the original LNO particles.

Summarizing the results from XRD, SEM, EDXS and TEM the reaction scheme given in Fig. 5 can be derived. The CCO in vicinity of the LNO partially decomposes to $Ca_3Co_2O_6$, CoO and O_2 during the sintering process at 1173 K. Usually, this decomposition of CCO only occurs at temperatures exceeding roughly 1200 K [8,9,54], wherefore the presence of LNO seems conditional. The LNO on the other hand reacted mainly to the perovskite La(Co,Ni)O_3 and (Ni,Co)O. The formation of the perovskite is associated with an oxidation of the Ni in LNO and a structural change. The structural change from LNO to higher Ruddlesden-Popper phases ($La_{n+1}Ni_nO_{3n+1}$ with n> 1) is not yet fully understood [56,57]. However, the formation of the perovskite from LNO is proven to be possible as demonstrated by Adachi et al. [58] for post-sintering oxidation, where a high partial pressure of O_2 and additional NiO was necessary. Hence, the oxygen and the CoO formed by the

decompositon of CCO as well as the high porosity of the system could play an important role. The La:Ni ratio in the perovskite requires more Ni or less La in comparison to the LNO. The EDXS results showed that excess La was compensated with the introduction of Co and some Ni even segregated from the compound. The presence of (Ni,Co)O could be a result of the segregated Ni and the formed CoO.

3.2. Ceramic composite: thermoelectric properties

The analysis of the microstructure in section 3.1 confirmed the presence of several phases within the CCO/LNO ceramic composites, namely CCO, LNO, La(Co,Ni)O_3, $Ca_3Co_2O_6$ and marginal (Ni,Co)O. Their overall influence on the thermoelectric properties was determined by measuring the electrical conductivity σ, Seebeck coefficient α and heat conductivity λ of the CCO/LNO ceramic composites in Fig. 6.

Beginning with the electrical conductivity in Fig. 6a, increasing

Interface and Ni-rich phase
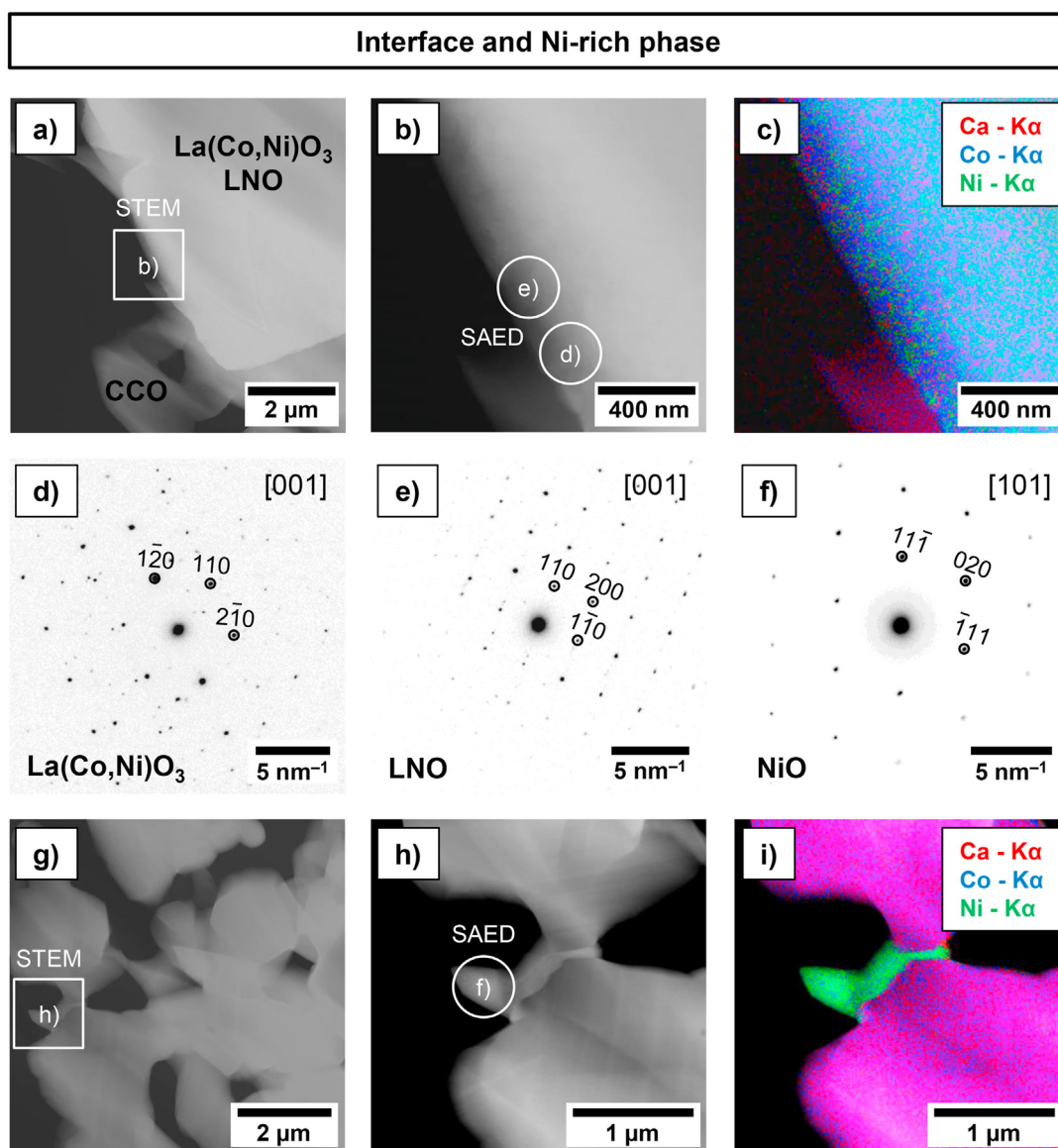
Fig. 4. Cross-sectional TEM characterization of the LNO-CCO interface and the Ni-rich phase within the sample of 5 wt% LNO. a,b) STEM annular dark-field micrographs of a large plate-like LNO grain surrounded by CCO. c) EDXS mapping of the CCO-LNO interface showing the homogeneous introduction of Co into the LNO. d,e) SAED patterns of the [001] zone axes of La(Co,Ni)O$_3$ and LNO with various different patterns indicating a polycrystalline material. f) SAED pattern of the Ni-rich phase NiO along the [101] zone axis. g,h) STEM annular dark-field micrographs of the NiO surrounded by CCO matrix. i) EDXS mapping of the NiO with no signs of Ni transport into the CCO.

values were measured for the 1–10 wt% LNO samples in comparison to CCO. At 1073 K the highest value of 76 S cm^{-1} was reached by the 5 wt% LNO composite, which is 17% higher than of CCO, but with further increasing amounts of LNO the electrical conductivity diminished. The improved values can be explained by the occurrence of the La(Co,Ni)O$_3$ phase, which is known for its comparatively high electrical conductivity [59]. The decreasing values after 5 wt% LNO could be caused by an unfavorable ratio of CCO to LNO leading to more contacts between LNO particles and more incomplete reactions. A deeper insight on the temperature dependency of the electrical conductivity is given in Fig. S5 in terms of an Arrhenius plot. A comparison of the activation energies of the electronic transport showed a general increase with higher amounts of LNO and a significant rise for the samples with 20 wt% and 40 wt% LNO. This means the transport behavior becomes more sensitive to temperature with increasing amounts of LNO. The nearly unchanged activation energy for the 1 wt% and 5 wt% samples could mean that low amounts do not hinder the electronic transport and can even be beneficial concerning

the electrically conductive La(Co,Ni)O$_3$ phase. A metallic-to-semiconducting transition at roughly 600 K was also noticed, which corresponds to reported values for CCO [60,61]. The Seebeck coefficient in Fig. 6b is usually inversely coupled with the electrical conductivity and is decreasing for all the CCO/LNO ceramic composites. This is caused by the lower Seebeck coefficients of the additional phases besides CCO. While LNO is also a *p*-type material, undoped LaNiO$_3$ is an *n*-type material with low negative Seebeck coefficients. Although, by substituting Ni with Co as it is the case here, the perovskite material becomes *p*-type and fits better with the CCO [59]. The reaction product Ca$_3$Co$_2$O$_6$ on the other hand has a higher Seebeck coefficient than the CCO but a lower electrical conductivity [62,63]. The combination of electrical conductivity and Seebeck coefficient results in the power factor shown in Fig. 6c. The 1 wt% and 5 wt% LNO samples both show a higher power factor while higher amounts of LNO lead to lower values. This means in both cases the increase in electrical conductivity overweighed the decrease of the Seebeck coefficient. For a complete picture of the
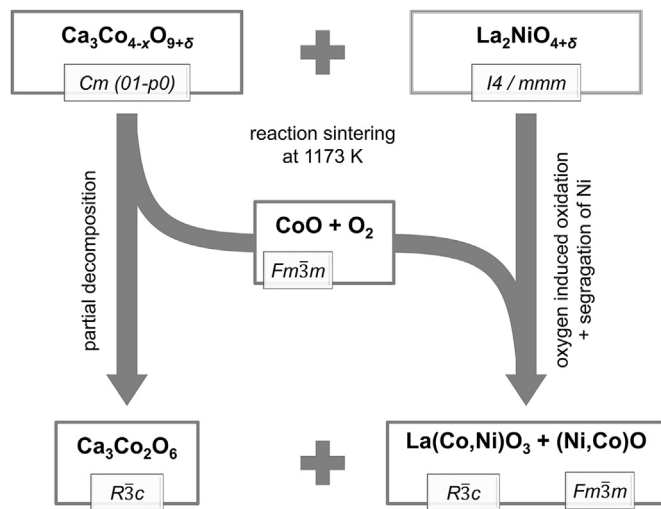
Fig. 5. Reaction scheme for the reaction sintering. The matrix CCO partially decomposes and the LNO mainly reacts to La(Co,Ni)O₃ and (Ni,Co)O.

thermoelectric properties, the heat conductivity λ is displayed in Fig. 6d. Overall, the heat conductivities of all measured samples are relatively low, which can be attributed to their high porosity [64]. The 1 wt% and 5 wt% samples show a decreased heat conductivity for temperatures below 873 K and 973 K respectively, while for the 10 wt% sample the values did deviate only slightly with the temperature and stay around the best value of CCO at 1073 K. This results in better average values for the CCO/LNO ceramic composites in comparison to CCO concerning the temperature range. Note that the values of λ above 573 K were fitted to the measurements parallel to the pressing direction, because the oxygen-helium atmosphere did not allow higher temperatures with the used setup (compare Fig. S6). A comparison of measurements in both

directions from the literature validates this method, as the temperature dependent trend is comparable [65,66]. The fact that all measured values for the heat conductivity parallel and perpendicular to the pressing direction differ proves anisotropy to some extent within the ceramic samples and the importance of combining the thermoelectric properties with the same direction.

The overall picture of the thermoelectric properties perpendicular to the pressing direction including two different Ioffe plots and the figure-of-merit zT is given in Fig. 7. The type-I Ioffe plot in Fig. 7a shows the power factor against the electrical conductivity. By this portrayal, the reason for the increased power factors of the 1 wt% and 5 wt% LNO samples gets obvious as the electrical conductivity increases. The type-II Ioffe plot in Fig. 7b on the other hand shows the thermal properties in terms of entropy conductivity Λ against the electrical conductivity. The minimum value of CCO could not be lowered in the ceramic composites, but the decreasing maximum value resulted in a better average value. The figure-of-merit zT is the combination of power factor and entropy conductivity and displayed in Fig. 7c as a function of the temperature. The 1 wt% LNO sample showed a higher power factor, but the increased entropy conductivity at 973 K and 1073 K led to a lower maximum zT than the CCO. The even higher power factor and slightly lower entropy conductivity of the 5 wt% LNO sample led to a similar maximum zT of 0.27 as the CCO. At the same time, the average zT was increased significantly by about 20% from 473 K to 1073 K. The average and maximum zT of the 10 wt% sample both decrease in comparison to CCO due to the shrinking power factor. Overall, the maximum zT could not be increased by the CCO/LNO ceramic composites, but a significantly higher average value was reached by the 5 wt% LNO sample for a temperature range of 373 K to 1073 K.

4. Conclusions

The combination of undoped $Ca_3Co_{-x}O_{9+\delta}$ and $La_2NiO_{4+\delta}$ in ceramic composites with varying ratios was investigated with respect to
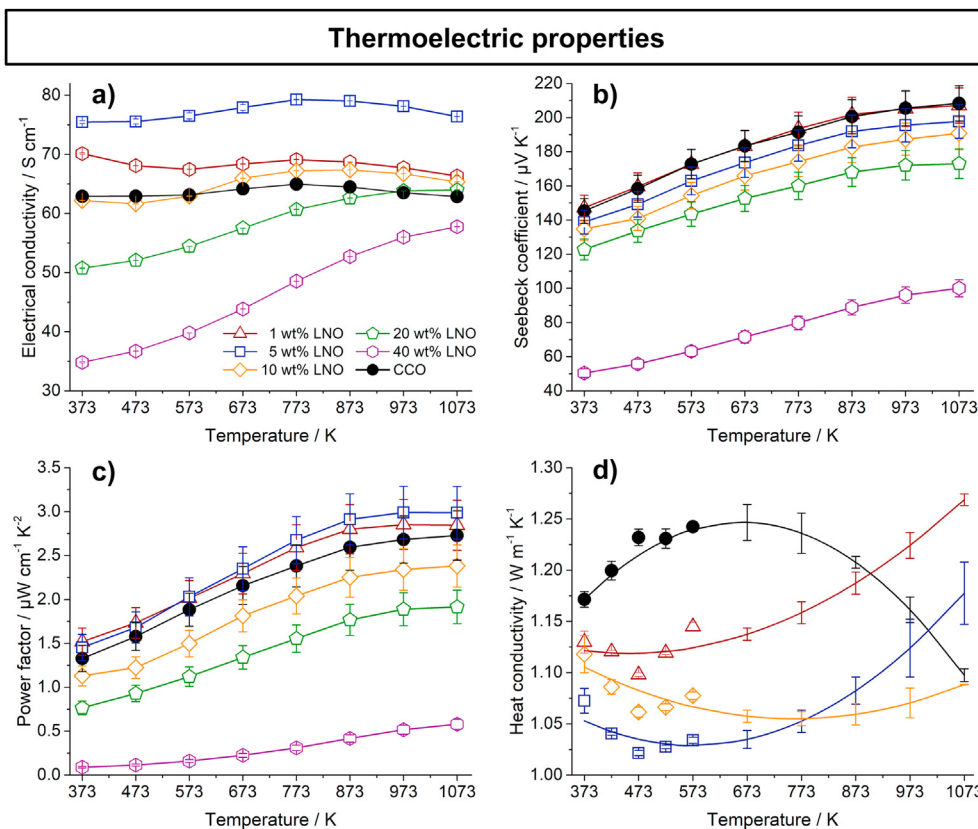

Fig. 6. Thermoelectric properties of the CCO/LNO ceramic composites perpendicular to the pressing direction in dependence on temperature with standard deviations. a) Electrical conductivity σ with increased values for the 1 wt% and 5 wt% LNO samples in comparison to CCO. b) Seebeck coefficient α with decreasing values for all ceramic composites. c) Power factor with increased values for the 1 wt% and 5 wt% LNO samples. d) Heat conductivity λ with increased values at high temperatures and decreased values at lower temperatures for the ceramic composites. Values above 573 K for the heat conductivity were gained by transferring fits and error bars for measurements parallel to the pressing direction (see Fig. S4).
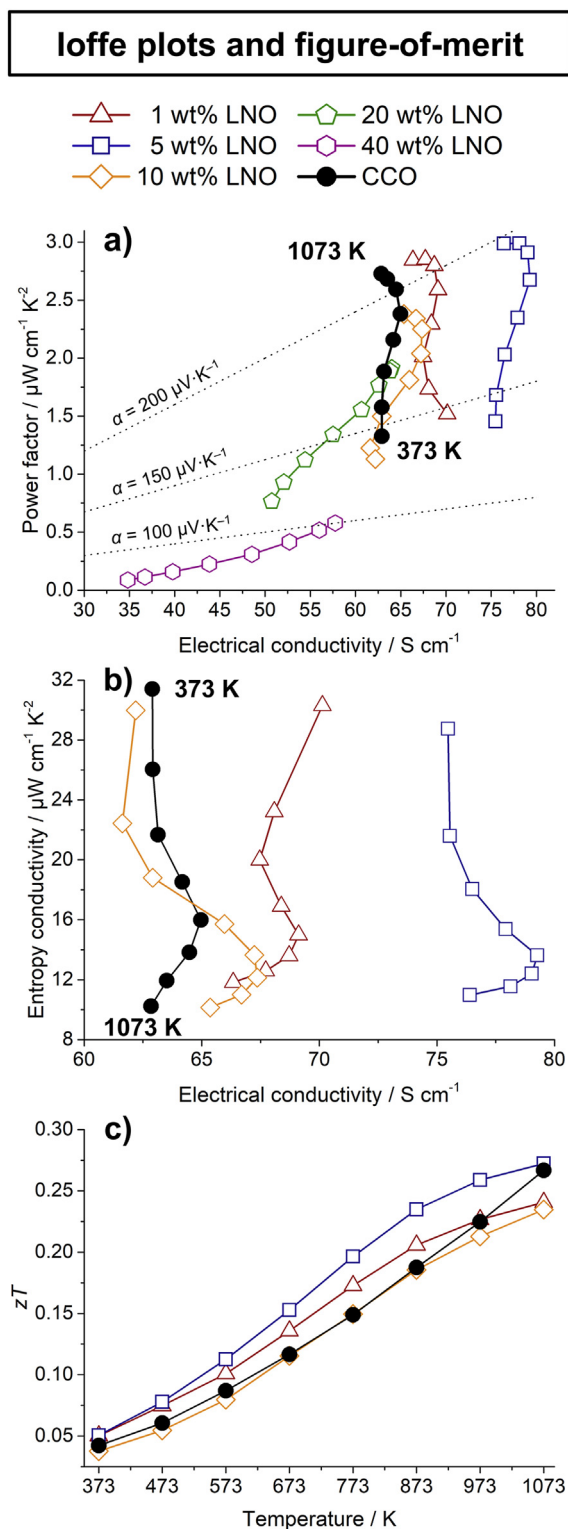
Fig. 7. Ioffe plots with 100 K temperature steps and figure-of-merit zT of the CCO/LNO ceramic composites. a) Type-I Ioffe plot with the power factor against the electrical conductivity σ. The samples with 1 wt% and 5 wt% LNO show a higher power factor than the CCO. b) Type-II Ioffe plot with the entropy conductivity Λ against the electrical conductivity σ. No composite has a lower entropy conductivity in comparison to CCO, but the overall range diminishes. c) Combined power factor and entropy conductivity in figure-of-merit zT against the temperature. The 5 wt% LNO sample shows the best properties with an increased average $\overline{ZT}$ in the temperature range of 373 K to 1073 K.

the thermoelectric properties. The choice of undoped $Ca_3Co_{4-x}O_{9+\delta}$ enabled the determination of reasons for changing thermoelectric properties, but future research could include a doped matrix or additional phases for possible improvements. Microstructure analysis by XRD, SEM, EDXS and TEM showed both compounds reacting with each other during the sintering, resulting in the partial formation of $Ca_3Co_2O_6$ and $La(Co,Ni)O_3$. The matrix material without contact to $La_2NiO_{4+\delta}$ was apparently not influenced and showed microtwins as stacking faults. The power factor of the 1 wt% and 5 wt% $La_2NiO_{4+\delta}$ composites were improved despite a diminishing Seebeck coefficient, because of the increased electrical conductivity resulting from the $La(Co,Ni)O_3$ phase. Thermal conductivity of these samples was not lowered at higher temperatures, but the average value was improved. This resulted in a similar maximum figure-of-merit zT of 0.27 for the best composite with 5 wt% $La_2NiO_{4+\delta}$ in comparison to pure $Ca_3Co_{4-x}O_{9+\delta}$, but the average $\overline{ZT}$ in the temperature range of 373 K to 1073 K could be increased by about 20%.

Declaration of interest

The authors declare that they have no known competing financial interests or personal relationships that could have appeared to influence the work reported in this paper.

Acknowledgements

Appendix A. Supplementary data

Supplementary data to this article can be found online at https ://doi.org/10.1016/j.oceram.2021.100103.

References

[1] G. Tan, L.-D. Zhao, M.G. Kanatzidis, Rationally designing high-performance bulk thermoelectric materials, Chem. Rev. 116 (2016) 12123–12149, https://doi.org/10.1021/acs.chemrev.6b00255.

[2] S.J. Poon, Recent advances in thermoelectric performance of half-Heusler compounds, Metals 8 (2018) 989, https://doi.org/10.3390/met8120989.

[3] J. Shuai, J. Mao, S. Song, Q. Zhang, G. Chen, Z. Ren, Recent progress and future challenges on thermoelectric Zintl materials, Mater. Today Phys. 1 (2017) 74–95, https://doi.org/10.1016/j.mtphys.2017.06.003.

[4] Q. Zhang, Y. Sun, W. Xu, D. Zhu, Organic thermoelectric materials: emerging green energy materials converting heat to electricity directly and efficiently, Adv. Mater. 26 (2014) 6829–6851, https://doi.org/10.1002/adma.201305371.

[5] Y. Yin, B. Tudu, A. Tiwari, Recent advances in oxide thermoelectric materials and modules, Vacuum 146 (2017) 356–374, https://doi.org/10.1016/j.vacuum.2017.04.015.

[6] L.-D. Zhao, J. He, D. Berardan, Y. Lin, J.-F. Li, C.-W. Nan, N. Dragoe, BiCuSeO oxyselenides: new promising thermoelectric materials, Energy Environ. Sci. 7 (2014) 2900–2924, https://doi.org/10.1039/c4ee00997e.

[7] J.W. Fergus, Oxide materials for high temperature thermoelectric energy conversion, J. Eur. Ceram. Soc. 32 (2012) 525–540, https://doi.org/10.1016/j.jeurceramsoc.2011.10.007.

[8] E. Woermann, A. Muan, Phase equilibria in the system CaO-cobalt oxide in air, J. Inorg. Nucl. Chem. 32 (1970) 1455–1459, https://doi.org/10.1016/0022-1902(70)80631-5.

[9] N. Kanas, S.P. Singh, M. Rotan, M. Saleemi, M. Bittner, A. Feldhoff, T. Norby, K. Wiik, T. Grande, M.-A. Einarsrud, Influence of processing on stability, microstructure and thermoelectric properties of $Ca_3Co_{4-x}O_{9+\delta}$, J. Eur. Ceram. Soc. 38 (2018) 1592–1599, https://doi.org/10.1016/j.jeurceramsoc.2017.11.011.

[10] Y. Miyazaki, Crystal structure and thermoelectric properties of the misfit-layered cobalt oxides, Solid State Ionics 172 (2004) 463–467, https://doi.org/10.1016/j.ssi.2004.01.046.

[11] Y. Miyazaki, M. Onoda, T. Oku, M. Kikuchi, Y. Ishii, Y. Ono, Y. Morii, T. Kajitani, Modulated structure of the thermoelectric compound $[Ca_2CoO_3]_{0.62}CoO_2$, J. Phys. Soc. Jpn. 71 (2002) 491–497, https://doi.org/10.1143/JPSJ.71.491.

[12] H.U. Fuchs, A direct entropic approach to uniform and spatially continuous dynamical models of thermoelectric devices, Energy Harvesting and Systems 1 (2014), https://doi.org/10.1515/ehs-2014-0011.

[13] A. Feldhoff, Thermoelectric material tensor derived from the Onsager–de Groot–Callen model, Energy Harvesting and Systems 2 (2015), https://doi.org/10.1515/ehs-2014-0040.

[14] A. Feldhoff, Power conversion and its efficiency in thermoelectric materials, Entropy 22 (2020) 803, https://doi.org/10.3390/e22080803.

[15] M. Wolf, R. Hinterding, A. Feldhoff, High power factor vs. high zT—A review of thermoelectric materials for high-temperature application, Entropy 21 (2019) 1058, https://doi.org/10.3390/e21111058.

[16] Q. Zhang, X. Ai, L. Wang, Y. Chang, W. Luo, W. Jiang, L. Chen, Improved thermoelectric performance of silver nanoparticles-dispersed Bi_2Te_3 composites deriving from hierarchical two-phased heterostructure, Adv. Funct. Mater. 25 (2015) 966–976, https://doi.org/10.1002/adfm.201402663.

[17] W. Liu, X. Yan, G. Chen, Z. Ren, Recent advances in thermoelectric nanocomposites, Nano Energy 1 (2012) 42–56, https://doi.org/10.1016/j.nanoen.2011.10.001.

[18] K. Kato, K. Kuriyama, T. Yabuki, K. Miyazaki, Organic-inorganic thermoelectric material for a printed generator, J. Phys. Conf. 1052 (2018), https://doi.org/10.1088/1742-6596/1052/1/012008, 012008.

[19] B. Zhang, J. Sun, H.E. Katz, F. Fang, R.L. Opila, Promising thermoelectric properties of commercial PEDOT:PSS materials and their Bi_2Te_3 powder composites, ACS Appl. Mater. Interfaces 2 (2010) 3170–3178, https://doi.org/10.1021/am100654p.

[20] N. Toshima, Recent progress of organic and hybrid thermoelectric materials, Synth. Met. 225 (2017) 3–21, https://doi.org/10.1016/j.synthmet.2016.12.017.

[21] M. Culebras, A. García-Barberá, J.F. Serrano-Claumarchirant, C.M. Gómez, A. Cantarero, Hybrids composites of NCCO/PEDOT for thermoelectric applications, Synth. Met. 225 (2017) 103–107, https://doi.org/10.1016/j.synthmet.2016.12.016.

[22] J.N. Coleman, M. Lotya, A. O'Neill, S.D. Bergin, P.J. King, U. Khan, K. Young, A. Gaucher, S. De, R.J. Smith, I.V. Shvets, S.K. Arora, G. Stanton, H.-Y. Kim, K. Lee, G.T. Kim, G.S. Duesberg, T. Hallam, J.J. Boland, J.J. Wang, J.F. Donegan, J.C. Grunlan, G. Moriarty, A. Shmeliov, R.J. Nicholls, J.M. Perkins, E.M. Grieveson, K. Theuwissen, D.W. McComb, P.D. Nellist, V. Nicolosi, Two-dimensional nanosheets produced by liquid exfoliation of layered materials, Science 331 (2011) 568–571, https://doi.org/10.1126/science.1194975.

[23] Q. Yao, L. Chen, W. Zhang, S. Liufu, X. Chen, Enhanced thermoelectric performance of single-walled carbon nanotubes/polyaniline hybrid nanocomposites, ACS Nano 4 (2010) 2445–2451, https://doi.org/10.1021/nn1002562.

[24] Y. Song, Q. Sun, L. Zhao, F. Wang, Z. Jiang, Synthesis and thermoelectric power factor of $(Ca_{0.95}Bi_{0.05})_3Co_4O_9$/Ag composites, Mater. Chem. Phys. 113 (2009) 645–649, https://doi.org/10.1016/j.matchemphys.2008.08.029.

[25] F. Kahraman, M.A. Madre, S. Rasekh, C. Salvador, P. Bosque, M.A. Torres, J.C. Diez, A. Sotelo, Enhancement of mechanical and thermoelectric properties of $Ca_3Co_4O_9$ by Ag addition, J. Eur. Ceram. Soc. 35 (2015) 3835–3841, https://doi.org/10.1016/j.jeurceramsoc.2015.05.029.

[26] Z. Shi, C. Zhang, T. Su, J. Xu, J. Zhu, H. Chen, T. Gao, M. Qin, P. Zhang, Y. Zhang, H. Yan, F. Gao, Boosting the thermoelectric performance of calcium cobaltite composites through structural defect engineering, ACS Appl. Mater. Interfaces 12 (2020) 21623–21632, https://doi.org/10.1021/acsami.0c03297.

[27] M. Wolf, K. Menekse, A. Mundstock, R. Hinterding, F. Nietschke, O. Oeckler, A. Feldhoff, Low thermal conductivity in thermoelectric oxide-based multiphase composites, J. Electron. Mater. 48 (2019) 7551–7561, https://doi.org/10.1007/s11664-019-07555-2.

[28] M. Bittner, N. Kanas, R. Hinterding, F. Steinbach, D. Groeneveld, P. Wemhoff, K. Wiik, M.-A. Einarsrud, A. Feldhoff, Triple-phase ceramic 2D nanocomposite with enhanced thermoelectric properties, J. Eur. Ceram. Soc. 39 (2019) 1237–1244, https://doi.org/10.1016/j.jeurceramsoc.2018.10.023.

[29] Y. Wang, Y. Sui, J. Cheng, X. Wang, W. Su, Comparison of the high temperature thermoelectric properties for Ag-doped and Ag-added $Ca_3Co_4O_9$, J. Alloys Compd. 477 (2009) 817–821, https://doi.org/10.1016/j.jallcom.2008.10.162.

[30] S. Saini, H.S. Yaddanapudi, K. Tian, Y. Yin, D. Magginetti, A. Tiwari, Terbium ion doping in $Ca_3Co_4O_9$: a step towards high-performance thermoelectric materials, Sci. Rep. 7 (2017) 44621, https://doi.org/10.1038/srep44621.

[31] S. Li, R. Funahashi, I. Matsubara, K. Ueno, S. Sodeoka, H. Yamada, Synthesis and thermoelectric properties of the new oxide materials $Ca_{3-x}Bi_xCo_4O_{9+\delta} < x < 0.75$), Chem. Mater. 12 (2000) 2424–2427, https://doi.org/10.1021/cm000132r.

[32] F. Delorme, P. Diaz-Chao, F. Giovannelli, Effect of Ca substitution by Fe on the thermoelectric properties of $Ca_3Co_4O_9$ ceramics, J. Electroceram. 40 (2018) 107–114, https://doi.org/10.1007/s10832-018-0109-2.

[33] D. Wang, L. Chen, Q. Yao, J. Li, High-temperature thermoelectric properties of $Ca_3Co_4O_{9+\delta}$ with Eu substitution, Solid State Commun. 129 (2004) 615–618, https://doi.org/10.1016/j.ssc.2003.11.045.

[34] N.V. Nong, C.-J. Liu, M. Ohtaki, High-temperature thermoelectric properties of late rare earth-doped $Ca_3Co_4O_{9+\delta}$, J. Alloys Compd. 509 (2011) 977–981, https://doi.org/10.1016/j.jallcom.2010.09.150.

[35] M. Shikano, R. Funahashi, Electrical and thermal properties of single-crystalline $(Ca_2CoO_3)_{0.7}CoO_2$ with a $Ca_3Co_4O_9$ structure, Appl. Phys. Lett. 82 (2003) 1851–1853, https://doi.org/10.1063/1.1562337.

[36] D.J. Bergman, O. Levy, Thermoelectric properties of a composite medium, J. Appl. Phys. 70 (1991) 6821–6833, https://doi.org/10.1063/1.349830.

[37] D.J. Bergman, L.G. Fel, Enhancement of thermoelectric power factor in composite thermoelectrics, J. Appl. Phys. 85 (1999) 8205–8216, https://doi.org/10.1063/1.370660.

[38] R. Hinterding, Z. Zhao, C. Zhang, A. Feldhoff, Anisotropic growth of $La_2NiO_{4+\delta}$: influential pre-treatment in molten-flux synthesis, J. Cryst. Growth 523 (2019) 125135, https://doi.org/10.1016/j.jcrysgro.2019.06.021.

[39] T. Klande, K. Efimov, S. Cusenza, K.-D. Becker, A. Feldhoff, Effect of doping, microstructure, and CO_2 on $La_2NiO_{4+\delta}$-based oxygen-transporting materials, J. Solid State Chem. 184 (2011) 3310–3318, https://doi.org/10.1016/j.jssc.2011.10.019.

[40] V. Kharton, A. Yaremchenko, E. Tsipis, A. Valente, M. Patrakeev, A. Shaula, J. Frade, J. Rocha, Characterization of mixed-conducting $La_2Ni_{0.9}Co_{0.1}O_{4+\delta}$ membranes for dry methane oxidation, Appl. Catal. Gen. 261 (2004) 25–35, https://doi.org/10.1016/j.apcata.2003.10.028.

[41] S.-Y. Jeon, M.-B. Choi, J.-H. Hwang, E.D. Wachsman, S.-J. Song, Electrical conductivity and thermoelectric power of $La_2NiO_{4+\delta}$, J. Electrochem. Soc. 158 (2011) B476, https://doi.org/10.1149/1.3559186.

[42] V. Pardo, A.S. Botana, D. Baldomir, Enhanced thermoelectric response of hole-doped $La_2NiO_{4+\delta}$ from ab initio calculations, Phys. Rev. B 86 (2012), https://doi.org/10.1103/PhysRevB.86.165114.

[43] C.G.S. Pillai, A.M. George, Thermal conductivity of La_2CuO_4, La_2NiO_4, and Nd_2CuO_4 in the semiconducting and metallic phases, Int. J. Thermophys. 7 (1986) 1091–1100, https://doi.org/10.1007/BF00502380.

[44] M. Burriel, J. Santiso, M.D. Rossell, G. van Tendeloo, A. Figueras, G. Garcia, Enhancing total conductivity of $La_2NiO_{4+\delta}$ epitaxial thin films by reducing thickness, J. Phys. Chem. C 112 (2008) 10982–10987, https://doi.org/10.1021/jp7101622.

[45] W. Paulus, A. Cousson, G. Dhalenne, J. Berthon, A. Revcolevschi, S. Hosoya, W. Treutmann, G. Heger, R. Le Toquin, Neutron diffraction studies of stoichiometric and oxygen intercalated La_2NiO_4 single crystals, Solid State Sci. 4 (2002) 565–573, https://doi.org/10.1016/S1293-2558(02)01299-2.

[46] M. Brunelli, M. Coduri, M. Ceretti, W. Paulus, Local apical oxygen disorder in oxygen rich $La_2NiO_{4.18}$, comparing neutron single crystal and n/X-PDF analysis from powder diffraction data, J. Phys. Appl. Phys. 48 (2015) 504009, https://doi.org/10.1088/0022-3727/48/50/504009.

[47] A.F. Ioffe, Semiconductor Thermoelements and Thermoelectric Cooling, first ed., Info-search Ltd., London, 1957.

[48] T. Janssen, A. Janner, A. Looijenga-Vos, P.M. De Wolff, International Tables for Crystallography: 9.8 Incommensurate and Commensurate Modulated Structures, vol. 3, Kluwer Acad. Publ, Dordrecht, 2004.

[49] T. Janssen, G. Chapuis, M. de Boissieu, Aperiodic Crystals: from Modulated Phases to Quasicrystals, Volume 20 of International Union of Crystallography Monographs on Crystallography, Oxford University Press, Oxford and New York, 2007.

[50] N. Kanas, G. Skomedal, T.D. Desissa, A. Feldhoff, T. Grande, K. Wiik, M.-A. Einarsrud, Performance of a thermoelectric module based on n-type $(La_{0.12}Sr_{0.88})_{0.95}TiO_{3-\delta}$ and p-type $Ca_3Co_{4-x}O_{9+\delta}$, J. Electron. Mater. 49 (2020) 4154–4159, https://doi.org/10.1007/s11664-020-08127-5.

[51] A.C. Masset, C. Michel, A. Maignan, M. Hervieu, O. Toulemonde, F. Studer, B. Raveau, J. Hejtmanek, Misfit-layered cobaltite with an anisotropic giant magnetoresistance: $Ca_3Co_4O_9$, Phys. Rev. B 62 (2000) 166–175, https://doi.org/10.1103/PhysRevB.62.166.

[52] K. Efimov, T. Klande, N. Juditzki, A. Feldhoff, Ca-containing CO_2-tolerant perovskite materials for oxygen separation, J. Membr. Sci. 389 (2012) 205–215, https://doi.org/10.1016/j.memsci.2011.10.030.

[53] C.B. Carter, Electron diffraction from microtwins and long-period polytypes, Philos. Mag. A 50 (1984) 133–141, https://doi.org/10.1080/01418618408244217.

[54] D. Sedmidubský, V. Jakeš, O. Jankovský, J. Leitner, Z. Sofer, J. Hejtmánek, Phase equilibria in Ca–Co–O system, J. Solid State Chem. 194 (2012) 199–205, https://doi.org/10.1016/j.jssc.2012.05.014.

[55] G. Constantinescu, A.R. Sarabando, S. Rasekh, D. Lopes, S. Sergiienko, P. Amirkhizi, J.R. Frade, A.V. Kovalevsky, Redox-promoted tailoring of the high-temperature electrical performance in $Ca_3Co_4O_9$ thermoelectric materials by metallic cobalt addition, Materials 13 (2020), https://doi.org/10.3390/ma13051060.

[56] N. Gauquelin, T.E. Weirich, M. Ceretti, W. Paulus, M. Schroeder, Long-term structural surface modifications of mixed conducting $La_2NiO_{4+\delta}$ at high temperatures, Monatshefte für Chemie - Chemical Monthly 140 (2009) 1095–1102, https://doi.org/10.1007/s00706-009-0146-2.

[57] R. Sayers, S.J. Skinner, Evidence for the catalytic oxidation of $La_2NiO_{4+\delta}$, J. Mater. Chem. 21 (2011) 414–419, https://doi.org/10.1039/c0jm02419h.

[58] Y. Adachi, N. Hatada, K. Hirota, M. Kato, T. Uda, Preparation of pure and fully dense lanthanum nickelates $La_{n+1}Ni_nO_{3n+1}$ (n = 2, 3, ∞) by post-sintering oxidation process, J. Am. Ceram. Soc. 102 (2019) 7077–7088, https://doi.org/10.1111/jace.16611.

[59] P. Migiakis, J. Androulakis, J. Giapintzakis, Thermoelectric properties of $LaNi_{1-x}Co_xO_3$ solid solution, J. Appl. Phys. 94 (2003) 7616, https://doi.org/10.1063/1.1629393.

[60] Y.-H. Lin, J. Lan, Z. Shen, Y. Liu, C.-W. Nan, J.-F. Li, High-temperature electrical transport behaviors in textured $Ca_3Co_4O_9$-based polycrystalline ceramics, Appl. Phys. Lett. 94 (2009), https://doi.org/10.1063/1.3086875, 072107.

[61] G. Constantinescu, S.M. Mikhalev, A.D. Lisenkov, D.V. Lopes, A.R. Sarabando, M.C. Ferro, T.F.d. Silva, S.A. Sergiienko, A.V. Kovalevsky, Prospects for electrical performance tuning in $Ca_3Co_4O_9$ materials by metallic Fe and Ni particles additions, Materials 14 (2021), https://doi.org/10.3390/ma14040980.

[62] M. Tahashi, K. Ogawa, M. Takahashi, H. Goto, Effect of compositional ratio of cobalt to calcium on crystal phase and thermoelectric properties of oxide thermoelectric material composed of sintered $Ca_3Co_4O_9$/$Ca_3Co_2O_6$ mixture, J. Ceram. Soc. Jpn. 121 (2013) 444–447, https://doi.org/10.2109/jcersj2.121.444.

[63] N. Kanas, S. Singh, M. Rotan, T. Desissa, T. Grande, K. Wiik, T. Norby, M.-A. Einarsrud, Thermoelectric properties of $Ca_3Co_{2-x}Mn_xO_6$ (x = 0.05, 0.2, 0.5, 0.75, and 1), Materials 12 (2019) 497, https://doi.org/10.3390/ma12030497.

[64] M. Bittner, L. Helmich, F. Nietschke, B. Geppert, O. Oeckler, A. Feldhoff, Porous $Ca_3Co_4O_9$ with enhanced thermoelectric properties derived from sol–gel synthesis, J. Eur. Ceram. Soc. 37 (2017) 3909–3915, https://doi.org/10.1016/j.jeurceramsoc.2017.04.059.

[65] D. Kenfaui, B. Lenoir, D. Chateigner, B. Ouladdiaf, M. Gomina, J.G. Noudem, Development of multilayer textured $Ca_3Co_4O_9$ materials for thermoelectric generators: influence of the anisotropy on the transport properties, J. Eur. Ceram. Soc. 32 (2012) 2405–2414, https://doi.org/10.1016/j.jeurceramsoc.2012.03.022.

[66] C.-H. Lim, W.-S. Seo, S. Lee, Y.S. Lim, J.-Y. Kim, H.-H. Park, S.-M. Choi, K.H. Lee, K. Park, Anisotropy of the thermoelectric figure of merit (ZT) in textured $Ca_3Co_4O_9$ ceramics prepared by using a spark plasma sintering process, J. Kor. Phys. Soc. 66 (2015) 794–799, https://doi.org/10.3938/jkps.66.794.